HHS Public Access

Author manuscript

Adv Funct Mater. Author manuscript; available in PMC 2022 November 14.

Published in final edited form as:

Adv Funct Mater. 2022 June 17; 32(25): . doi:10.1002/adfm.202112045.

Scalable Thousand Channel Penetrating Microneedle Arrays on Flex for Multimodal and Large Area Coverage BrainMachine Interfaces

Sang Heon Lee,
Integrated Electronics and Biointerfaces Laboratory, Department of Electrical and Computer Engineering, University of California San Diego, CA 92093, USA

Martin Thunemann,
Biomedical Engineering Department, Boston University, Boston, MA 02215, USA

Keundong Lee,
Integrated Electronics and Biointerfaces Laboratory, Department of Electrical and Computer Engineering, University of California San Diego, CA 92093, USA

Daniel R. Cleary,
Integrated Electronics and Biointerfaces Laboratory, Department of Electrical and Computer Engineering, University of California San Diego, CA 92093, USA

Department of Neurological Surgery, University of California San Diego, La Jolla, CA 92093, USA

Karen J. Tonsfeldt,
Integrated Electronics and Biointerfaces Laboratory, Department of Electrical and Computer Engineering, University of California San Diego, CA 92093, USA

Department of Obstetrics, Gynecology, and Reproductive Sciences, Center for Reproductive Science and Medicine, University of California San Diego, La Jolla, CA 92093, USA

Hongseok Oh,
Integrated Electronics and Biointerfaces Laboratory, Department of Electrical and Computer Engineering, University of California San Diego, CA 92093, USA

Farid Azzazy,
Integrated Electronics and Biointerfaces Laboratory, Department of Electrical and Computer Engineering, University of California San Diego, CA 92093, USA

Youngbin Tchoe,

sdayeh@ece.ucsd.edu .

Author Contributions

S.A.D. conceived and led the project. S.H.L. fabricated the SiMNAs, participated in animal experiments and analyzed the results. K.L., F.A., Y.G.R., A.T. contributed to the fabrication and characterization of the SiMNs. M.T., S.H.L., K.K., and A.D. conducted the mouse experiments and data analysis. D.R.C., K.J.T., S.H.L., and Y.T. conducted the rat animal experiments. A.M.B. contributed to the electrophysiology hardware and L.H. to the recordings. H.O. and Y.T. contributed to the data analysis. All authors discussed the results and contributed to the manuscript writing.

Supporting Information

Supporting Information is available from the Wiley Online Library or from the author.

Conflict of Interest

The authors declare no conflict of interest.

Integrated Electronics and Biointerfaces Laboratory, Department of Electrical and Computer Engineering, University of California San Diego, CA 92093, USA

Andrew M. Bourhis,
Integrated Electronics and Biointerfaces Laboratory, Department of Electrical and Computer Engineering, University of California San Diego, CA 92093, USA

Lorraine Hossain,
Integrated Electronics and Biointerfaces Laboratory, Department of Electrical and Computer Engineering, University of California San Diego, CA 92093, USA

Graduate Program of Materials Science and Engineering, University of California San Diego, La Jolla, CA 92093, USA

Yun Goo Ro,
Integrated Electronics and Biointerfaces Laboratory, Department of Electrical and Computer Engineering, University of California San Diego, CA 92093, USA

Atsunori Tanaka,
Integrated Electronics and Biointerfaces Laboratory, Department of Electrical and Computer Engineering, University of California San Diego, CA 92093, USA

Graduate Program of Materials Science and Engineering, University of California San Diego, La Jolla, CA 92093, USA

Kıvılcım Kılıç,
Biomedical Engineering Department, Boston University, Boston, MA 02215, USA

Anna Devor,
Biomedical Engineering Department, Boston University, Boston, MA 02215, USA

Athinoula A. Martinos Center for Biomedical Imaging, Department of Radiology, Harvard Medical School, Massachusetts General Hospital, Charlestown, MA 02129, USA

Shadi A. Dayeh
Integrated Electronics and Biointerfaces Laboratory, Department of Electrical and Computer Engineering, University of California San Diego, CA 92093, USA

Graduate Program of Materials Science and Engineering, University of California San Diego, La Jolla, CA 92093, USA

Abstract

The Utah array powers cutting-edge projects for restoration of neurological function, such as BrainGate, but the underlying electrode technology has itself advanced little in the last three decades. Here, advanced dual-side lithographic microfabrication processes is exploited to demonstrate a 1024-channel penetrating silicon microneedle array (SiMNA) that is scalable in its recording capabilities and cortical coverage and is suitable for clinical translation. The SiMNA is the first penetrating microneedle array with a flexible backing that affords compliancy to brain movements. In addition, the SiMNA is optically transparent permitting simultaneous optical and electrophysiological interrogation of neuronal activity. The SiMNA is used to demonstrate reliable recordings of spontaneous and evoked field potentials and of single unit activity in

chronically implanted mice for up to 196 days in response to optogenetic and to whisker air-puff stimuli. Significantly, the 1024-channel SiMNA establishes detailed spatiotemporal mapping of broadband brain activity in rats. This novel scalable and biocompatible SiMNA with its multimodal capability and sensitivity to broadband brain activity will accelerate the progress in fundamental neurophysiological investigations and establishes a new milestone for penetrating and large area coverage microelectrode arrays for brain–machine interfaces.

Keywords

arrays; brain; flexible; microneedles; microwires; thousand channels; transparent

1. Introduction

Neural interface technologies that enable recording of broadband activity are anticipated to revolutionize neuroprosthetics by restoring communication and motor control in patients with neurological injuries, for use with neurotherapies for patients with epilepsy, movement disorders, and for use with neurodegenerative and neuropsychiatric disrupted cognitive processes.[1] To record broadband activity including single units, electrodes that penetrate the cortex (penetrating electrodes) are usually used.[2–5] Such electrodes have been successfully utilized in intracortical brain computer interfaces (iBCI),[6,7] the localization and pathophysiology of seizures,[8,9] movement disorder therapeutics,[10–12] and in primary research on cognitive processes in the human brain.[13–15] However, such electrodes are often highly rigid and can therefore cause damage since they do not move with the brain, and when they fail, it is often attributable to connector and material issues related to rigidity.[16] More recent studies confirmed that the chronic tissue response is due to tethering forces of the connecting wires.[17] Multiport[18] and multisite Utah arrays[18,19] were also introduced to enhance the covered area and recording resolution of the platform, and electrical recording and stimulation capabilities were further modified by the application of iridium oxide.[20] The Utah array manufacturing process comprises Si dicing and bulk micromachining steps with a glass backing,[21] and recently with flexible polyethylene glycol (PEG) backing.[22] Each microneedle is hand-wired with insulated gold wire bonding.[22] Multimodality of Utah arrays was achieved by simply replacing one of the electrodes with an optrode[23,24] or fabricating the device entirely on transparent silicate glass for optogenetic stimulation and recording,[25,26] but these approaches are still based on rigid backplane, which hinders clear optical visualization of the implantation site.[18]

To overcome these limitations, new electrode technologies are evolving. Ultrathin flexible threads can reliably record brain activity across cortical depths and cause minimal scarring within the cortical tissue.[27,28] Implanting arrays made of neural threads requires advanced robotic implanters.[29] Similarly, thin and bendable carbon fiber probes induce minimal scarring[30] and allow single unit recordings though those have been mostly hand-assembled without a monolithic integration scheme yet.[31] Thermally drawn polymer fibers that enable neural recording, optical stimulation, and drug delivery were introduced, but they were limited to small implantation area with a few recording channels per device.[32] Recently, bundled microwire arrays have been used to massively scale the number of

recording channels through integration with high-definition complementary metal oxide semiconductor (CMOS) acquisition circuits,[33] and were scaled to 65 536 channels in the Argo system.[34] However, there are concerns for implanting the 65 536 channels of the Argo system into the brain because of the significant volumetric damage to the brain structure and as a result, it has so far been implemented for surface recordings in sheep.[34]

Here we introduce a novel silicon microneedle array (SiMNA) on thin, transparent, and flexible substrates that is scalable to thousands of channels and allows the simultaneous optical and electrophysiological intervention in the chronic setting. Such an advancement is timely, because it was demonstrated recently that vision was restored to nonhuman primates with 16 independent Utah arrays (total of 1024 silicon microneedles) that provided the required distribution of channels over relatively large cortical coverage.[35] The SiMNAs readily satisfy large cortical coverage—with compliancy to brain movements—and with custom distribution of the location of microwires, their diameters, and their pitch. We utilized bulk and surface micromachining techniques in novel combinations[36] and controlled the microscale electrochemical interface to achieve low electrochemical impedances using platinum nanomesh (PtNM) contacts.[37] We discuss fabrication and development of implantation procedures of the SiMNAs in benchtop experiments. We also demonstrate their broadband electrophysiological recording capabilities, as well as compatibility with two-photon imaging, optogenetic electrophysiological interrogations in the chronic setting using a proof-of-concept 32-channel SiMNA in mice. We then demonstrate the recording capabilities of the 1024-channel SiMNA in the acute rat animal experiments demonstrating high spatiotemporal mapping in rat cortex.

2. Results

2.1. A new Fabrication Process for Scalable SiMNAs on Flex, their Integration, and Benchtop Characterization

The definition of the SiMNA can be accomplished by plasma etching for relatively short Si microneedles (SiMNs) in the range of 10–200 μm, or a combination of dicing, plasma, and wet etching for taller microneedles. Our fabrication procedure is discussed in detail in the Experimental Section; and Figures S1, S2, S11, and S12 (Supporting Information). Briefly, the procedure involved the definition of Ni etch-masks on the front side of a double-side polished Si wafer for microneedle etching, and the back-side alignment to such masks and the definition of ohmic contacts and metallization traces embedded in polyimide layers on the back side of the Si wafer. The microneedle tip has a diameter of ≈10 μm and was coated with ≈0.5 μm thick Platinum–Silver (Pt-Ag) alloy underneath the Ni mask. After the microneedle etching, the Ag is dissolved to form a Pt nanomesh (PtNM) as the interface material; the PtNM increases the active surface area of the Pt due to its porous morphology as shown in Figure 1a. Figure 1b illustrates the high aspect ratio of a single SiMN, and the cross-sectional image of the underlying structure obtained by focused ion beam (FIB) sectioning. The cross-section is composed of ≈10 μm thick polyimide layer which acts as the main supporting substrate for the SiMNs. Additionally, a 1 μm thick parylene-C layer, which is deposited by isotropic chemical vapor deposition, fully encapsulates the SiMN device including the backside of the substrate and the sidewalls of the SiMN except for

the SiMN tip which is exposed by an O_2 plasma etching step in recessed photoresist. The fabricated device is then bonded to a custom printed circuit board (PCB) with zero-insertion-force (ZIF) connector which electrically connects the device to the recording system via flexible flat cable (FFC, Figure 1g). A custom 3D-printed headpost (Figure 1g) encases the PCB and secures the device on the mouse head with the custom titanium head frame as illustrated in Figures 2a and 3a. For maintaining a chronic optical access, we bonded the array with transparent, ultraviolet-curable glue (Norland Optical Adhesive 61) to the inner glass surface of the optical cranial window[38] with 3 mm inner diameter, 5 mm outer diameter, and total thickness of ≈450 μm (Figure 1h). The device mounted on the window was then implanted as a single assembly onto the primary somatosensory cortex of the left hemisphere in mice expressing Channelrhodopsin-2 fused to enhanced yellow fluorescent protein (ChR2-EYFP) in excitatory neurons (Emx1-Cre; Ai32 mice) using a protocol described in the Experimental Section; and Figure S3 (Supporting Information). This implantation procedure was optimized to enable full penetration of all SiMNs as validated by two-photon imaging. Figure 1j shows the top (*xy*) view as well as *xz* and *yz* cross-sections of a two-photon image stack where fluorescence is due to ChR2-EYP-expressing neurons and black shadows indicate SiMNs inserted into the tissue.

The small diameter of penetrating needles and fibers[30] minimize tissue damage but their native high electrochemical impedance which increases as the diameter decreases can impede their recording and stimulation capabilities. The impedance can be lowered by coating the SiMN tip with either; 1) a titanium/nickel (Ti/Ni) stack on the Si surface, followed by electrodeposition of novel conductive polymers such as poly(3,4-ethylenedioxythiophene) (PEDOT:PSS) on the topmost Ni layer, or 2) a metal stack of Cr/Pt atop the Si, followed by deposition of PtNM on the topmost Pt layer, in which either Ti or Cr for each method makes an ohmic contact to the n+ Si surface. Our investigation (Figures S4 and S5, Supporting Information) demonstrated better uniformity and yield for the monolithically integrated PtNM in comparison with either galvanostatic and potentiostatic electrodeposition of PEDOT:PSS. The electrochemical impedance magnitude and phase spectra in Dulbecco's phosphate-buffered saline (DPBS) are shown in Figure 1e,f, respectively, and contrast those before (red curve, Si tip) and after (blue curve, PtNM tip) coating the SiMN tips with PtNM. At 1 kHz, the average impedance of a SiMN with the PtNM tip was 643 ±208 kΩ, which is nearly an order of magnitude lower than the average impedance of 5.03 ±3.41 MΩ for the bare SiMN (Figure 1e). The 1 kHz in vivo impedance was monitored for three independent implantations (mouse #1, 2, and 3) for up to 137 days and was generally higher than at the benchtop, as expected (Figure 1o). The overall 1 kHz average impedance fluctuated below the 1.5 MΩ bar[39] which was suitable for high signal-to-noise ratio (SNR) recordings as will be demonstrated next. Notably, with their small diameter that is comparable to the 7 μm diameter carbon fibers,[30] our SiMNAs exhibited minimal tissue response for tissue analyzed 73 or 78 days after implantation (Figure 1k–n). The visual inspection of coronal, or cross-sectional sections (Figure 1k–n) of cortex stained to visualize cell nuclei (DAPI), neurons (NeuN antibody), astrocytes (GFAP antibody), and microglia (Iba-1) showed minor increase in astrocyte and microglial reactivity, comparable to what is expected from craniotomy and dura mater removal[40–42] performed for implantation of the device, but did not show noticeable change

in neuronal density when compared to the unexposed hemisphere in the same animal. Figure S6 (Supporting Information) shows a large field of view for a stained coronal section used for immunohistochemistry of chronic implantation of SiMNA on Flex.

2.2. Two-Photon Imaging and In Vivo Electrophysiological Recordings of Optogenetic Photostimulation-Evoked Responses in Anesthetized Mice

With optical access afforded by the flexible and transparent substrate backing of the penetrating SiMNAs, we were able to perform two-photon imaging through the array as illustrated in Figure 2a–c. Figure 2a shows a schematic illustration of our setup and Figure 2b shows the top view of the array implanted on the barrel cortex with clear visibility of the blood vessels underneath the SiMNA on flex. The small size of penetrating electrodes promoted insertion and minimized bleeding. Figure 2c is a magnified view of one of the microneedles that is penetrating into the cortical tissue adjacent to a surface venule without puncturing the blood vessel. To evaluate the capabilities of the SiMNAs in recording optogenetic photostimulation-evoked local field potentials, we targeted a 5 ms 450 nm laser light pulse at the cortical region covered by the 32-channel SiMNA using two different laser intensities (0.3 and 1.8 mW). The average SNR and standard deviation of unfiltered signals from all 32 channels in response to the 1.8 mW photostimulation were taken from days 11, 21, and 196, in vivo (Figure 2d). The average SNR for all 32 channels was 24.33 ± 12.04 in response to a laser beam that is focused in the center of the array. Figure 2e shows the SNR change of unfiltered responses from four representative channels in the center of the array with the same 1.8 mW photostimulation. The largest average SNR recorded on the same implantation model was 66.31 ± 57.13 for a photostimulation power up to 18.7 mW (Figure S7a,b, Supporting Information). For four selected channels at the center of the array, the SNR initially increased and experienced less variation after day 27 to reach a level between 40 and 50 on day 196. In order to demonstrate the multimodal capability of the SiMNAs, the same implantation model went through sensory-evoked electrophysiological recording under air puff stimulation from 41 to 137 days postimplantation (Figure S7b,c, Supporting Information). The average SNR of unfiltered responses from all 32 channels was 7.25 ±3.67, with some representative channels like Ch27 (with average SNR of 10.20 ±10.67 throughout day 41 to day 137) consistently showing higher SNR over time than other channels.

The 1.8 mW laser excitation power elicited well-resolved local field potentials (LFPs, < 250 Hz) and multiunit activity (250–3000 Hz) as shown in Figure 2f, where spontaneous multiunit activity (MUA) firing was also prevalent even after 196 days after implantation. The 0.3 mW laser excitation power did not evoke activity in the same recording session on the same animal. By focusing the laser beam to two different locations relative to the 32-channel SiMNA (indicated by light blue circles in Figure 2g–j), the location of the maximal responsive channels shifted accordingly for both LFP (Figure 2g,h) and MUA (Figure 2i,j). The comparison between premortem and postmortem photostimulation-evoked responses shown in Figure S7e,f (Supporting Information), further validated the electrophysiological recording.

2.3. Electrophysiological Recording of Sensory Evoked Responses and the Detection of Single Units in Awake Mice

We performed electrophysiological recordings of sensory stimulation-evoked responses in head-fixed awake mice. The whiskers on the right side of the mouse, contralateral to the implanted left hemisphere, were stimulated by deflection with an air puff (26 psi, one 5 ms pulse per trial, Figure 3a). Figure 3b shows a stack of trial-averaged filtered LFP and MUA responses from all SiMNs where the 22–28 ms poststimulus response is highlighted with a light-blue box. All response times for whisker stimulation reported in this work include the time it takes for air to flow through the stimulation tubing. Figure 3c provides magnified view of this average filtered data for a single, representative channel, in which the rectified MUA reveals the two key stages in the sensory stimulation-evoked response. The first response, highlighted with a red arrow, represents the initial sensory response to the air puff at 23 ms poststimulus, similar to previously reported response times on various rodent models.[43,44] The second response, highlighted with a green arrow, represents cortical activity due to the mouse whisking in response to the air puff in agreement with previously reported reflexive whisking evoked by sensory stimulation.[45,46] The whisking response started around ≈70 ms poststimulus as filmed in the video recording of the mouse motion and corresponded to the negative peak in the LFP response (Figure S8, Supporting Information). Note that, as shown in Figure S8b (Supporting Information), the temporal resolution of motion detection from video recording (20 or 40 Hz) was much lower than that of electrophysiological recordings (20 kHz), which leads to the impression that the motion initiated earlier than the electrophysiological responses.

The SiMNAs were also capable of recording single unit activity. To avoid influence of motion artifacts, we isolated single units during spontaneous activity in the awake mouse. Figure 3d illustrates example units and respective interspike interval (ISI) histograms detected from a single SiMN (see also Figure S9, Supporting Information). Other SiMNs in the same array detected between 2 and 9 units per channel from the same recording (Figure 3e,f). The recorded units from the SiMNA were independent from each other, confirmed by comparing the spike firing in raster plots of single units detected in four neighboring channels (Figure S9b–d, Supporting Information). The average SNR and standard deviation of all 32 channels in response to air puff stimulation were taken from days 27, 41, and 54, in vivo (Figure 3g). The average SNR for SUAs recorded for all 32 channels was 10.08 ±2.18 (Figure 3g). Figure 3I; and Figure S10 (Supporting Information) demonstrate SiMNA was able to reliably record SUA/MUA throughout the duration of the chronic implantation. The waveform of the detected units of a given channel changes with the number of days in vivo, which suggests that SiMNA has potentials as a tool for behavioral studies in chronic platforms. Finally, the spatiotemporal mapping capabilities of the SiMNA is illustrated in Figure 3h for the time duration highlighted by the light blue box of Figure 3b. The MUA response recorded with higher sensitivity on the left part of the array is initiated at the top left and moves toward the lower channels as time progresses. This MUA response also correlates with the LFP response that is initiated at the top-left corner of the SiMNA, and propagates toward the bottom-right of the array. These broadband high spatiotemporal resolution recordings demonstrate the capabilities of our SiMNA for fundamental and applied neurophysiological investigations.

2.4. A 1024-Channel SiMNA on Flex for Large Cortical Coverage Brain–Machine Interfaces

To illustrate the flexibility of the fabrication process in attaining high channel counts and taller SiMNAs that can reach deeper cortical layers, we prepared a 1024-channel individually addressable SiMNAs on flex (400 μm needle-to-needle spacing, 32 × 32) with cortical coverage area of 12.8 × 12.8 mm^2 (Figure 4a). The array is supported by the same 10 μm thick polyimide substrate that is encapsulating the metal leads. We combined the fabrication processes conventionally used for the Utah array with our double-side alignment, selective etching, and flexible substrates to attain cone-shaped SiMNAs with a sharp tip (see the Experimental Section; and Figures S11 and S12, Supporting Information). The height of the resulting SiMNs was ≈300 μm, with exposed tips for ≈50–100 μm down from the tip, that were also coated with PtNM, whereas the rest of the array was passivated with 2 μm thick parylene-C (Figure 4b).

The tapered shape and increased height of the SiMNs improved the mechanical stability during handling and insertion, and the sharp tip permitted easier insertion into the cortex. Figure 4c shows an optical image of the implanted array in the rat cortex. To minimize surgical complications in the anesthetized rat model, we implanted part of the 1024 SiMNAs in one hemisphere (green, 672 SiMNs), while the other SiMNAs rested on top of the rat skull (red, 352 SiMNs) as illustrated schematically in Figure 4d. The average SNR and standard deviation of LFP responses from the measured 672 channels were 9.76 ± 13.66 (Figure 4e). The average SNR was comparable to that recorded from the 32-channel SiMNA and the high standard deviation value also indicates highly localized activity. The sensory stimulation was delivered on all contralateral (left side of the rat) whiskers via air puff (40 psi, 5 ms duration). The colormaps of the air puff stimulation-evoked responses showed clear indication of broad LFP activation (Figure 4g), and more localized high gamma (HG) activation (Figure 4h). The colormap of the high pass filtered data (HPF) in the range of 250–3000 Hz was substantially more localized despite some large saturation from artifacts in the left side of the array (Figure 4i). Figure 4j–l shows all filtered waveforms from medial (M)-lateral (L), and anterior (A)-posterior (P) cross-sections from the colormaps in Figure 4g,h, and i, respectively. As the frequency range increases, it is clear that the average responses were much more localized, especially in the M-L cross-section. The LFP colormaps in Figure S13a (Supporting Information) further validated the spatiotemporal characteristics of the stimulation-evoked LFP which initiates around 35 ms poststimulus, similar to previously reported time stamp of 30 ms,[47] near the barrel cortex that is in the center of the successfully implanted SiMNs and propagates outwards and diminishes between 120 and 160 ms poststimulus. We also recorded with air puff stimulation on the anesthetized rat's hindlimb instead of the whiskers as control which evoked no LFPs, further confirming the validity of the whisker stimulation-evoked responses (Figure S13b, Supporting Information). To the best of our knowledge, this is the highest channel count of penetrating microneedle array that is ever monolithically fabricated, and notably in this case on a flexible substrate, and utilized in in vivo electrophysiological recordings.

3. Discussion

We implemented a flexible and scalable penetrating SiMNA. Additionally, the polyimide substrate for the SiMNA is transparent for photostimulation at a 450 nm wavelength in agreement with prior studies.[48] We demonstrated that our novel SiMNA allow simultaneous optical and electrophysiological interrogations and can record the broadband brain activity: This development permits novel investigations of large-scale cortical neuronal activity that require penetrating electrodes with broad area coverage with capacity of recording single unit activity and optical access that is previously not attained. We have also demonstrated the capability of the SiMNA to record with high spatiotemporal resolution broad band activity over centimeter scale brain areas: This development is crucial for expanding the reach of penetrating arrays in brain–machine interfaces to offer higher degrees of freedom in motor or sensory transduction available with the large area coverage. The 100 μm tall SiMNA causes minimal scarring and permitted chronic recordings up to 6 months. However, we did not assess the tissue response to the acutely implanted 1024-channel SiMNA. The additional penetration of thousands of longer microneedles into the brain may evoke tissue response well beyond that we observed on the 32-channel SiMNA.

Our monolithic fabrication process paves a new path for the relatively low cost, mass production of a hybrid platform of penetrating and flexible electrode arrays, similar to how Utah array demonstrated wafer-scale fabrication of penetrating microelectrode arrays.[49] In this work, we devised a fabrication technique that allows researchers to freely customize the density, height, and shape of the penetrating microelectrode arrays on a flexible substrate to meet the clinical/electrophysiological requirements for various in vivo studies. Microelectrodes with sharp tips previously demonstrated in vivo intracellular recording,[50] but were limited by small channel counts. Scalable microneedle array realized in this work promises possible in vivo intracellular recording with large area coverage.

Chronic recording with the 1024-channel SiMNAs, which requires large animal studies and compact connectorization, has not been demonstrated in this work. In order to translate the chronic recording platform from 32-channel SiMNAs to 1024-channel SiMNAs, a new round cranial window needs to be developed to allow a truly conformal implantation in which the flexible substrate wraps along the curvilinear surface of the cortex. We also did not pursue electrical stimulation to evoke motor responses. Wireless connection to the recording system[51,52] is another advance to facilitate the implementation of this platform on large animal models and incentivize clinical translation.

4. Conclusion

This work demonstrates the first functional microneedle array with flexible backing, its scalability to a thousand channels, and its use in chronic electrophysiological recordings from small animals. The fabrication processes developed here enable customization of the SiMNA density and microneedle height and establish a unique route for attaining large area coverage of implanted microneedles for brain–machine interfaces. Due to the transparency of the flexible substrate, optical stimulation, and imaging is possible and is demonstrated here with otpogenetic stimulation and 2-photon imaging in chronically implanted mice.

Finally, the scalability for large area coverage is demonstrated with a 1024-channel SiMNA that localized stimulus evoked responses in the rat brain. Our results illustrate unequivocally the power and the reach of the novel scalable fabrication processes with validation in small animals.

5. Experimental Section

32-Channel SiMNA on Flex Fabrication:

The fabrication begins with a 100 μm thick, double-side polished, n-type silicon wafer with low resistivity of 0.002–0.005 Ω cm for the preparation of reliable ohmic contact between the metal adhesion layers, chromium (Cr) and titanium (Ti), and the silicon microneedle at the top and bottom, respectively, later in the process. The wafer is cleaned using standard solvent cleaning procedure followed by acidic solution (acidic piranha, a mixture of sulfuric acid/hydrogen peroxide, H_2SO_4/H_2O_2) to remove organic contaminants, and the final buffered oxide etchant (BOE 6:1, Sigma-Aldrich) to remove the resulting oxide layer. The wafer is then spun-coated with 5 μm thick polyimide (PI2611, HD Microsystems), and cured in nitrogen-purged oven (HTCR, Carborlite) at a maximum temperature of 300 °C. 40 nm titanium (Ti) was electron-beam evaporated (BJD-1800 E-beam Evaporator 2, Temescal) on the polyimide side of the wafer to serve as the hard etch mask for the later step of dry etching of vias in the first layer of polyimide. Photolithography was performed to define the via sites to reach the Si surface and mask the rest of the underlying Ti layer, followed by reactive ion etching (RIE, Plasmalab 80+, Oxford Instruments) with SF_6/Ar to etch the Ti in the via sites. The remaining photoresist (NR9–3000PY, Futurrex, Inc.) was removed with solvents and the exposed polyimide on the via sites are RIE etched with O_2. The wafer was then dipped in BOE to remove the polyimide ashes from the RIE process on the vias, and the remaining Ti etch mask. Photolithography was performed again on the polyimide side of the wafer to define the ohmic contact and the metal leads. The wafer was descummed with O_2 (Plasma Etch 100, Plasma Etch, Inc.) and then treated with BOE to remove the native oxide on the Si surface at the via sites and swiftly loaded for electron-beam evaporation of the following: first layer of 20 nm Ti for ohmic contact with the Si, then 80 nm Ni which later serves as the etch stop layer for deep reactive ion etching (DRIE), and finally 10 nm Cr to prevent oxidation of the metal layers. The wafer was then transferred to Denton Discovery 18 Sputter System to sputter 250 nm Ti for conformal electrical connection between the proceeding metal stack at the vias and the metal leads on the surface of the polyimide. The polyimide side of the wafer is spin-coated and cured again with 5 μm thick polyimide to encapsulate the metal layers (Figure S1a, Supporting Information).

After RIE etching residual polymer residue and oxide on the exposed Si side of the wafer with O_2 and CHF_3/Ar, respectively, the wafer was flipped upside down for the novel backside-alignment process (MA6 Mask Aligner, Karl Suss) to photolithographically define another array of ohmic contacts, which in part, serves as the DRIE etch mask to form “sacrificial Si pillars” on the exposed Si side of the wafer. The wafer was descummed with O_2, the native oxide was removed on the Si surface with BOE, and then sputtered with 15 nm Cr for the ohmic contact, 100 nm Pt, and finally ≈0.5 μm Pt-Ag alloy was deposited

by cosputtering technique in which the power was set at 400 W for Ag, and 100 W for Pt (Figure S1b, Supporting Information).

The wafer was immediately transferred to an electron-beam evaporator to evaporate 10 nm Ti as the adhesion layer between Pt-Ag alloy and Ni, and finally 50 nm Ni to serve as the DRIE etch-mask layer later in the process (Figure S1c, Supporting Information). After lifting off residual metal stacks, the polyimide side of the wafer was carefully bonded to a carrier wafer (500 μm thick, single side polished Si wafer) with photoresist (NR9–6000PY, Futurrex, Inc.) then baked at 150 °C for 1 min. DRIE (Plasmalab 100, Oxford Instruments) was used to perform anisotropic 2-step etch process (Bosch process, or combination of isotropic plasma etch with SF_6, and passivation with C_4F_8) to etch Si and leaving an array of 100 μm tall, vertical SiMNs underneath the predefined Cr/Pt/Pt-Ag/Ti/Ni metal stack (Figure S1d, Supporting Information). During this process, the additional metal stack of Cr/Pt/Pt-Ag/Ti/Ni also leaves “sacrificial Si pillars” (Figure S2c–h, Supporting Information), defined around the actual Si micropillar array to be served as the electrodes. These additional protecting pillars assist with the fine control of the etch profile, or the tapering angle of the DRIE etched pillars, by modifying the density of the array.[50,53] These sacrificial pillars have relatively weaker bonding to the underlying polyimide substrate when compared to the actual SiMN electrode supported on the exposed metal contact at the base. This allows a simple process of breaking off the sacrificial pillars with a probe tip of a micromanipulator setup.

The device is then released from the carrier wafer and coated with 1 μm thick parylene-C layer (SCS Labcoter 2 Parylene Deposition System, Specialty Coating Systems) to passivate the entire device (Figure S1e, Supporting Information).

The device was remounted to a carrier wafer with the SiMNs facing up. The polyimide/parylene-C substrate of the device was slowly spin-coated with negative photoresist (NR9–6000PY, Futurrex, Inc.) and then baked without UV exposure. The photoresist layer was dipped in a resist developer (RD6, Futurrex, Inc.) for up to 10 s, much shorter than the usual photolithography process. This removes the thinner layer of photoresist at the tip of the SiMNs without exposing the other protected areas of the polymer substrate, allowing selective RIE with O_2 to remove the parylene-C layer only at the tip of the microneedles. The remaining oxidized photoresist is removed with the same resist developer to prevent residues which may occur from conventional solvent cleaning technique. The Ni mask at the exposed tip of the SiMNs was removed with Ni etchant (Ni etchant TFB, Transene Company, Inc.) and the underlying Ti layer was removed with BOE. Then the Pt-Ag was de-alloyed by removing the Ag component from the alloy with HNO_3 heated at 60 °C for 2 min which leaves the final PtNM electrode surface at the tip of the SiMNs (Figure S1f, Supporting Information).[37]

The device was again RIE etched while covering the array region with glass slides without damaging the SiMNs, and only exposing the electrical contact pads embedded in polymer substrate on the opposite end with regard to the SiMNA. Finally, the device was released from the carrier wafer and bonded with conductive epoxy (Silver Conductive Epoxy Adhesive, MG Chemicals) to a custom connector PCB.

1024-Channel SiMNA on Flex Fabrication:

The fabrication begins with a 500 μm thick, double side polished, n-type silicon wafer with low resistivity of 0.001–0.005 Ω cm for the preparation of reliable ohmic contact between the metal adhesion layer of Cr and the silicon microneedle at the top and bottom of the final SiMN later in the process. The wafer is cleaned using standard solvent cleaning procedure followed by buffered oxide etchant (BOE 6:1, Sigma-Aldrich) to remove the resulting oxide layer. The wafer is then spun-coated with 5 μm thick polyimide (PI2611, HD Microsystems), and cured in nitrogen-purged oven (HTCR, Carbolite) at maximum temperature of 300 °C. 50 nm Ti was electron-beam evaporated (BJD-1800 E-beam Evaporator, Temescal) on the polyimide side of the wafer to serve as the hard etch mask for the later step of dry etching of vias in the first layer of polyimide. Photolithography was performed with photoresist (NR9–3000PY, Futurrex, Inc.) to define the via sites and mask the rest of the underlying Ti layer, followed by reactive ion etching (RIE, Plasmalab 80+, Oxford Instruments) with SF_6/Ar to etch the Ti in the via sites. The remaining photoresist was removed with solvents (acetone) and the exposed polyimide on the via sites are RIE etched with O_2. The wafer was then dipped in BOE to remove the polyimide ashes from the RIE process on the vias, and the remaining Ti etch mask. Photolithography was performed again on the polyimide side of the wafer to define the ohmic contact and the metal leads. The wafer was descummed with O_2 (Plasma Etch 100, Plasma Etch, Inc.) and treated with BOE to remove the native oxide on the Si surface at the via sites and swiftly loaded to sputter (Discovery 18, Denton Vacuum) to deposit 15 nm Cr for ohmic contact with the Si, then 100 nm Pt for conformal electrical connection. The polyimide side of the wafer is spun-coated and cured again with 5 μm thick polyimide to encapsulate the metal layers (Figure S11a, Supporting Information).

After RIE etching of residual polymer residue and oxide on the exposed Si side of the wafer with O_2 and CHF_3/Ar, respectively, the wafer was flipped upside down for the novel backside-alignment process (MA6 Mask Aligner, Karl Suss) to photolithographically define a grid to serves as the alignment guidelines for the dicing step later in the process. The wafer was descummed with O_2, the native oxide was removed on the Si surface with BOE, and then electron-beam evaporated with 50 nm Ti (Figure S11b, Supporting Information).

The polyimide side of the wafer was bonded to a carrier wafer (500 μm thick, single side polished Si wafer) with photoresist (NR9–6000PY, Futurrex, Inc.) then baked at 150 °C for 1 min. The combined wafer was mounted to an automatic dicing saw system (DAD3220, Disco) for the dicing process. The dicing saw was aligned with the Ti grid on the top Si surface and was programmed to make partial cuts at blade feed speed of 0.5 mm s^{-1}, creating 470 μm deep, 300 μm wide trenches in between the micropillars, each with the tip area of around 100 × 100 μm^2. This forms a 58 × 58 array of Si micropillars of which the 32 × 32 array in the center are the SiMN electrodes in the final device. The surrounding micropillars which allows ease of handling and serve as the “buffer zone” during the later wet etch process for more uniform length of the final SiMN electrodes (Figure S11c, Supporting Information).

The diced wafer was unmounted from the dicing saw system and the Si micropillars were thinned down by isotropic dry etching with XeF_2 (XeF_2 Etcher, Xactix) until the micropillar

tip area was about 90 × 90 μm^2. The wafer was transferred for DRIE (Plasmalab 100, Oxford Instruments). The 2-step etch process (Bosch process, or combination of isotropic plasma etch with SF_6, and passivation with C_4F_8) etches away the thin, residual Si near the base of the Si micropillars to electrically isolate them from each other. The device was then released from the carrier wafer and the large Si pieces surrounding the array region were manually peeled off from the polyimide substrate. The Si micropillars were further sharpened with Si etchant solution (HF/HNO_3) for around 2–5 min, similar to the "static etch" utilized to fabricate Utah electrode arrays[54] (Figures S11d and S12, Supporting Information).

All surviving additional, electrically nonfunctional Si micropillars in the "buffer zone" are removed using the probe tip of the micromanipulator setup similar to the process described in the fabrication of the 32-channel device. The device was remounted to a carrier wafer with the SiMNs facing up by laminating the device on the carrier wafer spin-coated with negative photoresist (NR9–6000PY, Futurrex, Inc.) then baked without UV exposure. Four small (about 5 × 1.8 mm^2 each) 500 μm thick Si pieces were bonded with photoresist to form a square frame surrounding the array, on top of the polyimide substrate. Similar to the preparation of "selective RIE step" in the fabrication of 32-channel device, this allows thicker coating of photoresist for the SiMNs. The mounted device was again spun-coated twice with the same photoresist at slower spin speed of 1000 RPM, and a second spin-coat at 500 RPM, with 5 min vacuum and 5 min prebake in between each spin-coat. The wafer was then cured in an oven for 2 h at 80 °C, and dipped in a resist developer (RD6, Futurrex, Inc.) for up to 20 s with agitation. This removes the thinner layer of photoresist at the tip of the SiMNs without exposing the other areas coated with the photoresist. Any residual photoresist at the tips was descummed with O_2, the native oxide was removed on the Si surface with BOE, and then 15 nm Cr was sputtered for the ohmic contact, 100 nm Pt, and finally ≈0.5 μm Pt-Ag alloy was deposited by cosputtering technique in which the power was set at 400 W for Ag, and 100 W for Pt (Figures S11e and S12f, Supporting Information).

The device is released from the carrier wafer, and coated with 2 μm thick parylene-C layer (SCS Labcoter 2 Parylene Deposition System, Specialty Coating Systems) to passivate the entire device. The coated device was laminated to a carrier wafer with the same procedure detailed in the earlier steps of the fabrication. A custom etch mask was prepared using the laser cutter (ULS 3.5, Universal Laser Systems) to puncture holes in stencil film (2 Mil polyester tape with silicone adhesive, APT) which was temporarily mounted to the device. The punctured holes or vias on the stencil mask are aligned with the electrical contact pads region at the other end from the SiMN array. The polyimide/parylene-C layers embedding the contact pads were RIE etched with O_2 through the vias in the stencil mask, while other exposed regions were covered with glass sides without damaging the array region. The stencil mask was removed after the contact pads are fully exposed and the same multistep photoresist spin-coating technique used for Pt-Ag alloy deposition was performed to selectively RIE etch the parylene-C layer with O_2, that is passivating the tip of the SiMNs. Then the device was released from the carrier wafer, and the exposed Pt-Ag was dealloyed by removing the Ag component from the alloy with HNO_3 heated at 60 °C for 2 min which leaves the final PtNM electrode surface at the tip of the SiMNs. Finally, a timed RIE O_2

plasma etch is used to etch the passivating parylene C layer and the device is cut and bonded with conductive epoxy (Silver Conductive Epoxy Adhesive, MG Chemicals) to a custom connector PCB (Figure S14, Supporting Information).

Animal Procedures:

All experimental procedures were performed in accordance with the guidelines established by the UCSD Institutional Animal Care and Use Committee (IACUC) approved under protocol # S07360 for the mouse experiments in Prof. Devor's laboratory and protocol S S16020 for the rat experiments in Prof. Dayeh's laboratory. For mouse studies, 3 adult (age > 8 weeks) Emx1-Cre; Ai32 double transgenic (het/het) mice of either sex (JAX 005628 and 024109) on C57BL/6 background were used.[55,56] Surgical procedures were performed as previously described[57] with some modifications. Briefly, a 3 mm cranial window was implanted over the left barrel cortex (coordinates A-P 2 mm and L-R 3 mm relative to bregma). As a reference electrode, a microscrew was inserted above the cerebellum of the right hemisphere. For head fixation of the animals during recording procedures, a custom-designed headpost machined from titanium was attached. The headpost allows fixation of a custom connector PCB within a lightweight 3D-printed protective enclosure.

After surgery, animals were allowed to recover for 7–14 days before animals are habituated for head fixation.[58] Animals were anesthetized with Isoflurane, the headpost was fixed to the stage, and the recording equipment was connected. Then, anesthesia was discontinued, and animals woke up, while under head-restrain. Recording sessions were started that lasted for 30–60 min.

For the acute rat surgeries, male Sprague–Dawley rats (350–500 g) were initially anesthetized using 3–4% isofluorane and placed in a stereotaxic frame (Kopf). A craniotomy was made on the right skull extending from bregma ≈1 cm laterally and 1 cm posteriorly, exposing the right somatosensory cortex, including barrel cortex. The dura was carefully opened and retracted from the brain, and a small piece of saline-soaked gauze was placed over the brain until the implant was ready. The rat was transitioned from isofluorane to ketamine/xylazine (100 and 10 mg kg^{-1}, respectively) to establish light anesthesia for recording, with redosing every 20–30 min. Heart rate, core temperature, and blood oxygenation were continuously monitored during the experiment. Prior to recordings, selected whiskers were identified and marked in accordance to prior descriptions of barrel fields, and the remaining whiskers were cut short.[59] During the experiment, individual whiskers were stimulated with small, precise puffs of air using a mechanically and pneumatically powered system, to avoid artifact from electrical pulses (PicoSpritzer II, Parker Hannifin, NH).

Histology:

At the end of the study, animals were deeply anesthetized with 210 mg kg^{-1} pentobarbital (Fatal Plus) and transcardially perfused with 10 mL heparinized DPBS followed by 15 mL DPBS with 4% paraformaldehyde (PFA, prepared from 16% PFA stocks, Electron Microscopy Sciences). After perfusion, brains were extracted and placed in DPBS with 4% PFA overnight at 4 °C. Then, brains were transferred into water containing 20% sucrose

until further processing. The location of the craniotomy was highlighted by inserting a glass microneedle covered in carbon beads at four corners around the implantation site.

For immunofluorescence, the brain was paraffin embedded and sectioned at 5 μm (UCSD Tissue Technology Shared Resources). Every fourth section was processed for hematoxylin/eosin (H&E) staining. A subset of the remaining sections was rehydrated, and antigen retrieval performed using a Retriever 2100 (Electron Microscopy Sciences) in citrate buffer. Sections were washed and blocked in 0.5% goat serum in PBS-T (0.03% Triton-X) for 1 h. The sections were then incubated in primary antibodies in PBS-T (chicken anti-NeuN, 1:500, Sigma-Aldrich ABN91; Cy3-conjugated anti-GFAP, 1:1000, Sigma-Aldrich C9205; rabbit anti-Iba-1, 1:1000, Sigma-Aldrich ZRB1177) overnight. Sections were washed and incubated with secondary antibodies for 30 min (1:100; goat anti-chicken 488, Sigma-Aldrich SAB4600039; goat anti-rabbit 647, Sigma-Aldrich SAB2600184). After final washes, sections were air dried and cover-slipped with ProLong Gold with DAPI (Thermo-Fisher). Images were acquired at the UCSD Nikon Imaging Core using a Nikon Eclipse Ti2-E equipped with a DS-Qi2 CMOS camera, controlled by NIS-E-Elements (Nikon).

Two-Photon Imaging:

Procedures were similar to those described previously.[58] Briefly, fluorescein isothiocyanate (FITC)-labeled dextran (MW = 2 MDa, FD-2000S, Sigma), or Alexa Fluor 680 conjugated to amino-dextran (MW = 2 MDa, Finabio AD2000×100) in-house, was injected IV (50–100 μL of 5% w/v solution in phosphate-buffered saline) to visualize the vasculature. Images were obtained using an Ultima two-photon laser scanning microscopy system from Bruker Fluorescence Microscopy equipped with an Ultra II femtosecond Ti:Sapphire laser (Coherent) tuned to 950 nm for imaging of EYFP. For imaging of Alexa 680 Dextran, an Optical Parametric Oscillator (Chameleon Compact OPO, Coherent), pumped by the same Ti:Sapphire laser, was tuned to 1240 nm. EYFP and Alexa Fluor 680 were imaged using cooled GaAsP detectors (Hamamatsu, H7422P-40). A 4x objective (Olympus XLFluor4x/340, NA = 0.28) to obtain low-resolution images of the exposure was used. An 0.5-NA 20x objective water-immersion objective (Olympus UMPlanFI) was used for high-resolution imaging.

Optogenetic Photostimulation:

Optogenetic stimulation was performed with a 450 nm diode-pumped solid-state laser (Optoengine) either coupled to a 200 μm, 0.22 NA optical fiber (Thorlabs FG200UEA) or into the Ultima two-photon laser scanning microscopy. Pulses were controlled through Prairie View Software; a trigger signal in synchronization with the laser pulse was sent to the Intan recording system for synchronization.

Sensory Stimulation:

For sensory stimulation, each trial consisted of a single air puffs delivered to the lower bottom part of the contralateral whisker pad to avoid eye blink reflexes. In case of 1024-channel device on anesthetized rat model, contralateral hindlimb was also stimulated with the same air puff for comparison with the stimulation on whiskers. Air puffs were delivered through a pneumatic microinjector (Pneumatic PicoPump, World Precision Instruments)

controlled through a data acquisition system with custom-written MATLAB routines; a trigger signal in synchronization with the air puff was sent to the Intan recording system for synchronization.

Statistical Analysis of Electrophysiological Data:

The electrophysiological data were recorded as previously described[39] using a RHD2000 amplifier board and RHD2000 evaluation system (Intan Technologies). The sampling rate was 20 kHz. Data were analyzed in MATLAB using custom-written software. After import and conversion into MATLAB files, bandpass filter was applied at 1–250 Hz for local field potential activity, bandpass filter was applied at 250–3000 Hz for activity in the higher frequency band such as MUA and single units, trigger signals were detected, and further evaluation steps were performed.

The motion of the awake mouse was recorded using a CCD camera (Basler acA1920) upon illumination with a 940 nm LED (Thorlabs) at frame rate of 20 or 40 Hz, which was synchronized to electrophysiological data using the trigger signals recorded with the RHD2000 evaluation system. The video data were collected as individual frames using a custom MATLAB code which then calculated the standard deviation of brightness over time in images of the contralateral whisker pad region.

For single unit detection, the electrophysiological data that had lower than either 5% (mouse #6) or 10% (mouse #4) of the motion data were selected to prevent motion artifact affecting the spike sorting process. The selected data were exported to Offline Sorter (Plexon). Spikes were detected by setting the waveform length of 1500 μs, prethreshold period of 350 μs, dead time of 1150 μs, and then the threshold was set to −3 times standard deviations from mean of peak heights histogram,[60,61] automatic sorting using valley seeking scan mode.

For calculation of SNR, the average responses of N trials (N = 20 for 32-channel SiMNA, and N = 60 for 1024-channel SiMNA) by restricting the trial average window to 10 ms prestimulus, and to 1 s poststimulus were computed. The amplitude of the response ($V_{\text{pp-Response}}$) was extracted from the maximum and minimum voltages within the 0–1 s poststimulus, which was then divided by the baseline amplitude ($V_{\text{pp-baseline}}$) extracted from the last 50 ms of the same window (0.95–1 s poststimulus) in order to calculate the SNR

$$SNR_{\text{ch}} = \frac{V_{\text{pp-Response}}}{V_{\text{pp-baseline}}}$$

Data Availability Statement

The data that support the findings of this study are available from the corresponding author upon reasonable request.

Supplementary Material

Refer to Web version on PubMed Central for supplementary material.

Acknowledgements

This work was supported by the National Institutes of Health Award No. NIBIB DP2-EB029757, NINDS R01NS123655-01, and NINDS UG3NS123723-01 to S.A.D., and Nos. 1R01DA050159-01 and R01 MH111359-05 to A.D., the National Science Foundation Award No. 1728497 and CAREER No. 1351980 to S.A.D., and by the KAVLI Institute for Brain and Mind. The authors thank technical support from the nano3 cleanroom facilities at UC San Diego's Qualcomm Institute. This work was performed in part at the San Diego Nanotechnology Infrastructure (SDNI) of UC San Diego, a member of the National Nanotechnology Coordinated Infrastructure, which was supported by the National Science Foundation (Grant No. ECCS1542148). Tissue processing was performed by the UCSD Tissue Technology Shared Resource (No. P30 CA23100), and the authors thank the UCSD Nikon Imaging Core for microscope access. The authors acknowledge insightful discussions with Prof. Massoud L. Khraiche of the American University of Beirut, and Prof. Vikash Gilja of UC San Diego.

References

[1]. Cash SS, Hochberg LR, Neuron 2015, 86, 79. [PubMed: 25856488]

[2]. Fried I, Wilson CL, Maidment NT, Engel J Jr, Behnke E, Fields TA, Macdonald KA, Morrow JW, Ackerson L, J. Neurosurg 1999, 91, 697. [PubMed: 10507396]

[3]. Worrell GA, Gardner AB, Stead SM, Hu S, Goerss S, Cascino GJ, Meyer FB, Marsh R, Litt B, Brain 2008, 131, 928. [PubMed: 18263625]

[4]. Ulbert I, Halgren E, Heit G, Karmos G, J. Neurosci. Methods 2001, 106, 69. [PubMed: 11248342]

[5]. Nordhausen CT, Maynard EM, Normann RA, Brain Res. 1996, 726, 129. [PubMed: 8836553]

[6]. Hochberg LR, Serruya MD, Friehs GM, Mukand JA, Saleh M, Caplan AH, Branner A, Chen D, Penn RD, Donoghue JP, Nature 2006, 442, 164. [PubMed: 16838014]

[7]. Collinger JL, Wodlinger B, Downey JE, Wang W, Tyler-Kabara EC, Weber DJ, McMorland AJ, Velliste M, Boninger ML, Schwartz AB, Lancet 2013, 381, 557. [PubMed: 23253623]

[8]. Bragin A, Wilson CL, Staba RJ, Reddick M, Fried I, Engel J, Ann. Neurol 2002, 52, 407. [PubMed: 12325068]

[9]. Truccolo W, Donoghue JA, Hochberg LR, Eskandar EN, Madsen JR, Anderson WS, Brown EN, Halgren E, Cash SS, Nat. Neurosci 2011, 14, 635. [PubMed: 21441925]

[10]. MacMillan ML, Dostrovsky JO, Lozano AM, Hutchison WD, J. Neurophysiol 2004, 91, 1085. [PubMed: 14573552]

[11]. Bergman H, Deuschl G, Mov. Disord 2002, 17, S28. [PubMed: 11948753]

[12]. Engel AK, Moll CK, Fried I, Ojemann GA, Nat. Rev. Neurosci 2005, 6, 35. [PubMed: 15611725]

[13]. Chan AM, Dykstra AR, Jayaram V, Leonard MK, Travis KE, Gygi B, Baker JM, Eskandar E, Hochberg LR, Halgren E, Cereb.l Cortex 2013, 24, 2679.

[14]. Quiroga RQ, Kreiman G, Koch C, Fried I, Trends Cognit. Sci 2008, 12, 87. [PubMed: 18262826]

[15]. Kreiman G, Curr. Opin. Neurobiol 2007, 17, 471. [PubMed: 17703936]

[16]. Barrese JC, Rao N, Paroo K, Triebwasser C, Vargas-Irwin C, Franquemont L, Donoghue JP, J. Neural Eng 2013, 10, 066014. [PubMed: 24216311]

[17]. Ersen A, Elkabes S, Freedman DS, Sahin M, J. Neural Eng 2015, 12, 016019. [PubMed: 25605679]

[18]. Zheng X, Neural Interface: Frontiers and Applications, Springer, New York 2015.

[19]. Shandhi M, Leber M, Hogan A, Bhandari R, Negi S, in 2015 Transducers-2015 18th International Conference on Solid-State Sensors, Actuators and Microsystems (TRANSDUCERS), IEEE, New York 2015.

[20]. Negi S, Bhandari R, Rieth L, Solzbacher F, Sens. Actuators, B 2009, 137, 370.

[21]. Normann RA, Campbell PK, Jones KE, Three-dimensional electrode device, USA Patent 5,215,088, 1993.

[22]. Leber M, Bhandari R, Solzbacher F, Negi S, in 2017 19th International Conference on Solid-State Sensors, Actuators and Microsystems (TRANSDUCERS), IEEE, New York 2017.

[23]. Zhang J, Laiwalla F, Kim JA, Urabe H, Van Wagenen R, Song Y-K, Connors BW, Zhang F, Deisseroth K, Nurmikko AV, J. Neural Eng 2009, 6, 055007. [PubMed: 19721185]

[24]. Wang J, Wagner F, Borton DA, Zhang J, Ozden I, Burwell RD, Nurmikko AV, van Wagenen R, Diester I, Deisseroth K, J. Neural Eng 2011, 9, 016001. [PubMed: 22156042]

[25]. Abaya TVF, Diwekar M, Blair S, Tathireddy P, Rieth L, Solzbacher F, J. Biomed. Opt 2014, 19, 015006.

[26]. Abaya T, Diwekar M, Blair S, Tathireddy P, Rieth L, Solzbacher F, in 2012 International Conference on Optical MEMS and Nanophotonics, IEEE, New York 2012.

[27]. Luan L, Wei X, Zhao Z, Siegel JJ, Potnis O, Tuppen CA, Lin S, Kazmi S, Fowler RA, Holloway S, Sci. Adv 2017, 3, e1601966. [PubMed: 28246640]

[28]. Chung JE, Joo HR, Fan JL, Liu DF, Barnett AH, Chen S, Geaghan-Breiner C, Karlsson MP, Karlsson M, Lee KY, Neuron 2019, 101, 21. e25. [PubMed: 30502044]

[29]. Musk E, J. Med. Internet Res 2019, 21, e16194. [PubMed: 31642810]

[30]. Kozai TDY, Langhals NB, Patel PR, Deng X, Zhang H, Smith KL, Lahann J, Kotov NA, Kipke DR, Nat. Mater 2012, 11, 1065. [PubMed: 23142839]

[31]. Patel PR, Na K, Zhang H, Kozai TD, Kotov NA, Yoon E, Chestek CA, J. Neural Eng 2015, 12, 046009. [PubMed: 26035638]

[32]. Canales A, Jia X, Froriep UP, Koppes RA, Tringides CM, Selvidge J, Lu C, Hou C, Wei L, Fink Y, Nat. Biotechnol 2015, 33, 277. [PubMed: 25599177]

[33]. Obaid A, Hanna M-E, Wu Y-W, Kollo M, Racz R, Angle MR, Müller J, Brackbill N, Wray W, Franke F, Sci. Adv 2000, 6, eaay2789.

[34]. Sahasrabuddhe K, Khan AA, Singh AP, Stern TM, Ng Y, Tadić A, Orel P, LaReau C, Pouzzner D, Nishimura K, J. Neural Eng 2021, 18, 015002. [PubMed: 33624614]

[35]. Chen X, Wang F, Fernandez E, Roelfsema PR, Science 2020, 370, 1191. [PubMed: 33273097]

[36]. Shadi A, Azzazy F, Lee SH, Flexible penetrating cortical multi-electrode arrays, sensor devices and manufacturing methods. 2017.

[37]. Ganji M, Paulk AC, Yang JC, Vahidi NW, Lee SH, Liu R, Hossain L, Arneodo EM, Thunemann M, Shigyo M, Nano Lett. 2019, 19, 6244. [PubMed: 31369283]

[38]. Goldey GJ, Roumis DK, Glickfeld LL, Kerlin AM, Reid RC, Bonin V, Schafer DP, Andermann ML, Nat. Protoc 2014, 9, 2515. [PubMed: 25275789]

[39]. Thunemann M, Lu Y, Liu X, Kılıç K, Desjardins M, Vandenberghe M, Sadegh S, Saisan PA, Cheng Q, Weldy KL,Nat. Commun 2018, 9, 2035. [PubMed: 29789548]

[40]. Dorand RD, Barkauskas DS, Evans TA, Petrosiute A, Huang AY, Intravital 2014, 3, e29728. [PubMed: 25568834]

[41]. Drew PJ, Shih AY, Driscoll JD, Knutsen PM, Blinder P, Davalos D, Akassoglou K, Tsai PS, Kleinfeld D, Nat. Methods 2010, 7, 981. [PubMed: 20966916]

[42]. Guo D, Zou J, Rensing N, Wong M, PLoS One 2017, 12, e0170005. [PubMed: 28107381]

[43]. Honjoh T, Ji Z-G, Yokoyama Y, Sumiyoshi A, Shibuya Y, Matsuzaka Y, Kawashima R, Mushiake H, Ishizuka T, Yawo H, PLoS One 2014, 9, e93706. [PubMed: 24695456]

[44]. Reig R, Silberberg G, Neuron 2014, 83, 1200. [PubMed: 25155959]

[45]. Bellavance M-A, Takatoh J, Lu J, Demers M, Kleinfeld D, Wang F, Deschênes M, Neuron 2017, 95, e674.

[46]. Nguyen Q-T, Kleinfeld D, Neuron 2005, 45, 447. [PubMed: 15694330]

[47]. Ollerenshaw DR, Bari BA, Millard DC, Orr LE, Wang Q, Stanley GB, J. Neurophysiol 2012, 108, 479. [PubMed: 22514290]

[48]. Brosch M, Deckert M, Rathi S, Takagaki K, Weidner T, Ohl FW, Schmidt B, Lippert MT, J. Neural Eng 2020, 17, 046014. [PubMed: 32705997]

[49]. Bhandari R, Negi S, Solzbacher F, Biomed. Microdevices 2010, 12, 797. [PubMed: 20480240]

[50]. Hanein Y, Schabmueller C, Holman G, Luecke P, Denton D, Böhringer K, J. Micromech. Microeng 2003, 13, S91.

[51]. Schwarz DA, Lebedev MA, Hanson TL, Dimitrov DF, Lehew G, Meloy J, Rajangam S, Subramanian V, Ifft PJ, Li Z, Nat. Methods 2014, 11, 670. [PubMed: 24776634]

[52]. Zhou A, Santacruz SR, Johnson BC, Alexandrov G, Moin A, Burghardt FL, Rabaey JM, Carmena JM, Muller R, Nat. Biomed. Eng 2019, 3, 15. [PubMed: 30932068]

[53]. Kibler AB, Jamieson BG, Durand DM, J. Neurosci. Methods 2012, 204, 296. [PubMed: 22179041]

[54]. Campbell PK, Jones KE, Huber RJ, Horch KW, Normann RA, IEEE Trans. Biomed. Eng 1991, 38, 758. [PubMed: 1937509]

[55]. Gorski JA, Talley T, Qiu M, Puelles L, Rubenstein JL, Jones KR, J. Neurosci 2002, 22, 6309. [PubMed: 12151506]

[56]. Madisen L, Mao T, Koch H, m Zhuo J, Berenyi A, Fujisawa S, Hsu Y-WA, Garcia AJ, Gu X, Zanella S, Nat. Neurosci 2012, 15, 793. [PubMed: 22446880]

[57]. Desjardins M, Kılıç K, Thunemann M, Mateo C, Holland D, Ferri CG, Cremonesi JA, Li B, Cheng Q, Weldy KL, Biol. Psy-chiatry: Cognit. Neurosci. Neuroimaging 2019, 4, 533.

[58]. Uhlirova H, Kılıç K, Tian P, Thunemann M, Desjardins M, Saisan PA, Sakadžić S, Ness TV, Mateo C, Cheng Q, elife 2016, 5, e14315. [PubMed: 27244241]

[59]. Simons DJ, J. Neurophysiol 1978, 41, 798. [PubMed: 660231]

[60]. Christie BP, Tat DM, Irwin ZT, Gilja V, Nuyujukian P, Foster JD, Ryu SI, Shenoy KV, Thompson DE, Chestek CA, J. Neural Eng 2014, 12, 016009. [PubMed: 25504690]

[61]. Park J, Kim G, Jung S-D, IEEE Trans. Neural Syst. Rehabil. Eng 2017, 25, 2227. [PubMed: 28459692]

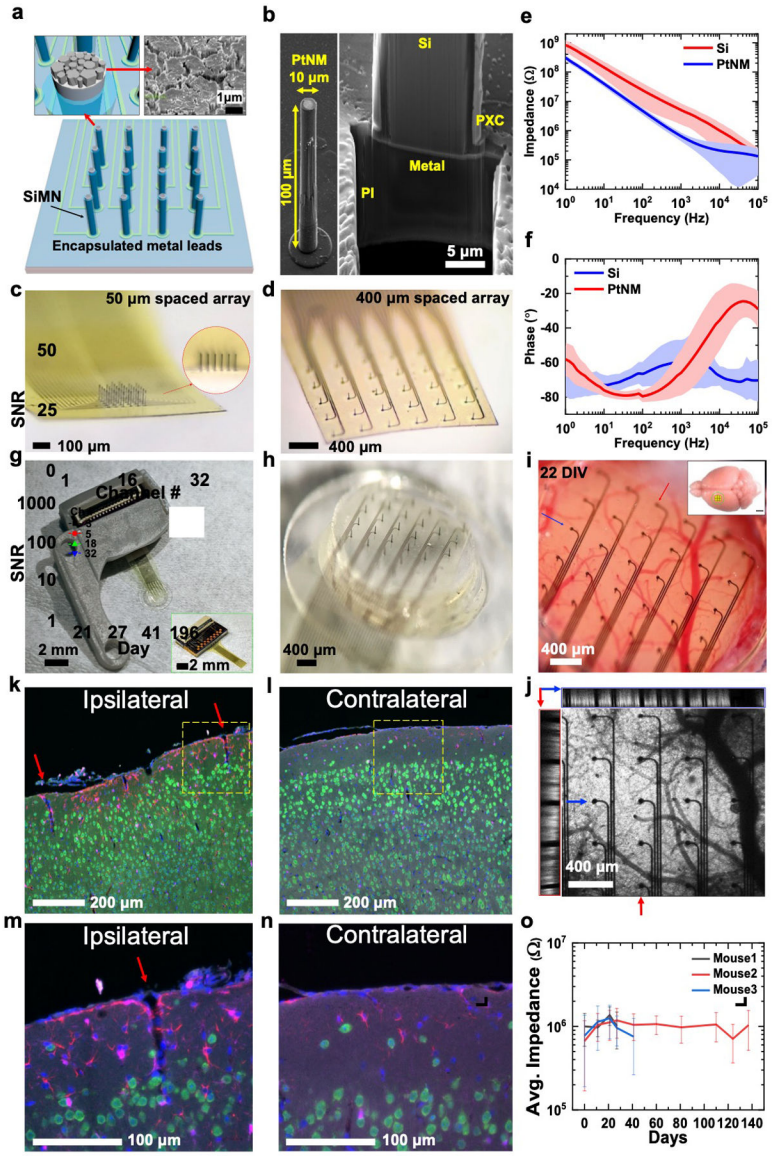

Figure 1.

32-channel silicon microneedle array on flexible substrate (SiMNA on flex) for multimodal recording. a) A schematic of a 32-channel SiMNA on flex with polyimide passivating the metal leads and parylene-C passivating the SiMNA (excluding the tips). Inset on the left shows magnified view of the exposed SiMN tip with PtNM coated on Si, and the inset on the right shows the scanning electron microscopy (SEM) image of the PtNM surface at the tip. b) SEM images (59.8° view) showing a single SiMN with height of 100 μm and diameter of about 10 μm (left), and the FIB-cut cross-section at the base of a single SiMN to demonstrate the underlying 10 μm thick flexible polyimide (PI) substrate supporting the metal lead and the SiMN that are passivated with 1 μm thick parylene-C layer (PXC). c) A magnified optical image of 32-channel SiMNA with 50 μm needle-to-needle spacing. The inset shows the magnified photograph taken from the side of the SiMNA. d) A magnified photograph of 32-channel SiMNA with 400 μm needle-to-needle spacing. e) Impedance

plotted against frequency for a Si needle with diameter of 10 μm before (red) and after (blue) coating with PtNM. The average impedance at 1 kHz was 643 ±208 kΩ for PtNM and 5.03 ±3.41 MΩ for Si surface. f) Phase angle plotted against frequency for a SiMN with diameter of 10 μm before (red) and after (blue) coating with PtNM. The average phase angle at 1 kHz was −66.0° ±13.2° for PtNM and −60.4° ±13.4° for Si surface, before PtNM coating. g) A photograph of the device mounted on 3D-printed custom headpost. Inset shows a photograph of a 32-channel SiMNA with 400 μm needle-to-needle spacing bonded to a custom connector PCB before mounting on 3D-printed custom headpost. h) A magnified photograph of the array region mounted on chronic cranial window before implantation. i) A magnified photograph of a 32-channel SiMNA implanted on mouse somatosensory cortex (22 days in vivo). Inset shows the approximate size of the craniotomy at the implantation site (scale bar, 2 mm). j) Two-photon image of the array from i). The left (red box) and the top (blue box) insets show the cross-sectional images taken from the vertical (red arrow, medial-lateral) and horizontal (blue arrow, posterior–anterior) sections. Fluorescence results from pan-neuronal ChR2-EYFP expression in Emx1-Cre; Ai32 mice. k–n) Fluorescence microscopy images of coronal tissue sections stained to visualize cell nuclei (DAPI, blue), neurons (NeuN antibody, green), astrocytes (GFAP antibody, red), and microglia (Iba1 antibody, magenta) from the SiMNA-implanted hemisphere (ipsilateral), and control hemisphere (contralateral) after 73 days in vivo. Red arrows indicate tissue penetration from single SiNM and yellow dashed boxes indicate the magnified regions in m) and n). o) Average impedance of electrically functional SiMNs plotted against days of chronic implantation in 3 different mouse brains.

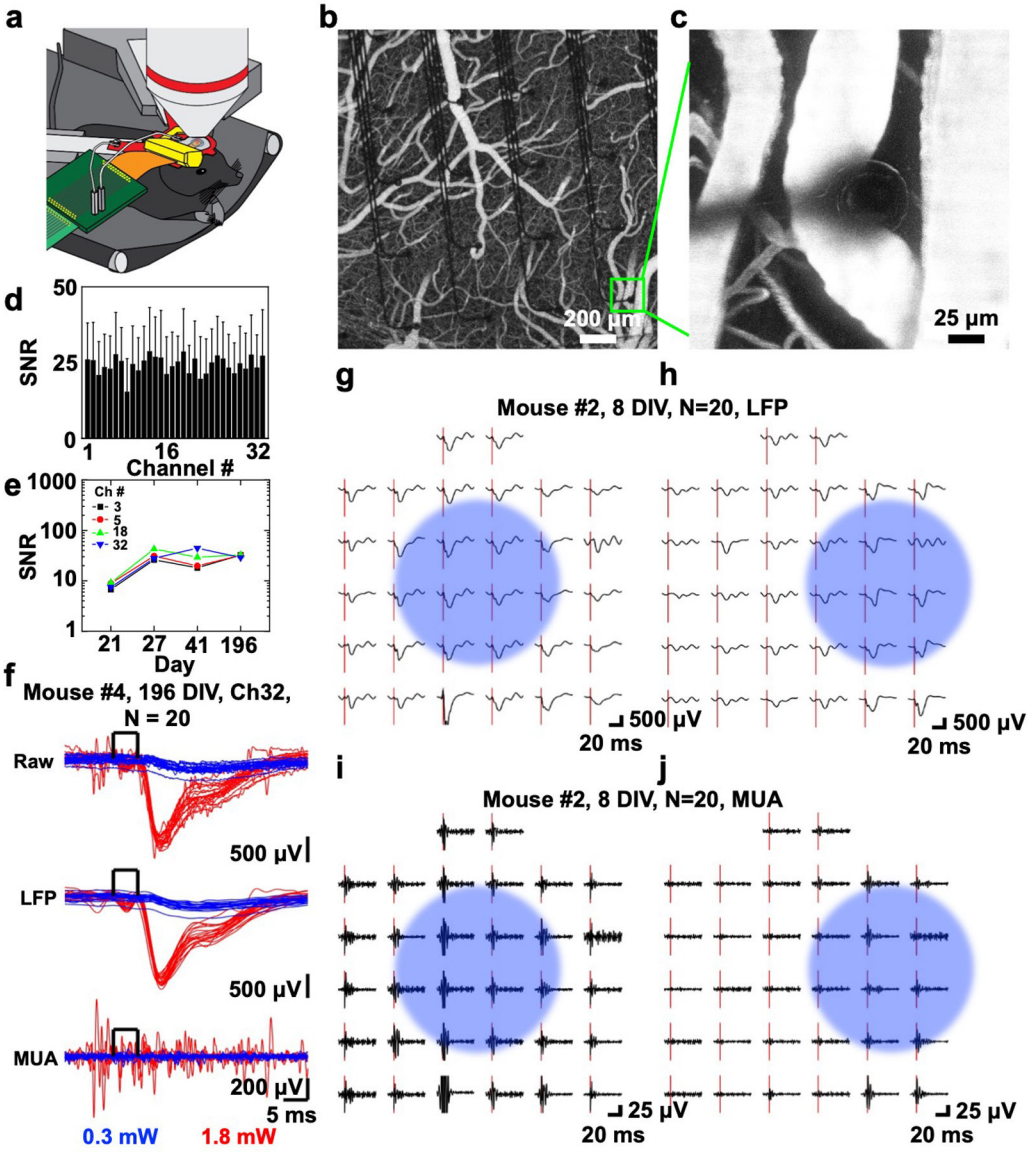

Figure 2.

In vivo optogenetic photostimulation-evoked responses. a) Schematic illustration of chronic in vivo optogenetic experiment setup showing microscope objective for optogenetic photostimulation (top), custom titanium head frame (red) supporting custom 3D-printed headpost (yellow), and PCB connector (green) leading to the recording system. b) Two-photon image of the 400 μm spacing 32-channel SiMNA on flex implanted on mouse somatosensory cortex after intravenous injection of Alexa 680-Dextran. c) A magnified two-photon image from the same device b) focused on a SiMN. d) Histogram of average SNR and standard deviation of 1.8 mW photostimulation-evoked responses (unfiltered) for 32 channels (up to 196 DIV). e) SNR change of four channels in the center of the SiMNA (up to 196 DIV). f) Stacks of optogenetic photostimulation-evoked electrical potentials from all individual trials ($N = 20$) from a single channel (Ch32) of a 400 μm spacing 32-channel SiMNA at 196 DIV. Raw and filtered data (LFP: 1–250 Hz, MUA: 250–3000 Hz) for 0.3

mW (blue) and 1.8 mW (red) 450 nm laser power for optogenetic photostimulation (5 ms square pulse). g–j) Average potential waveforms in response to optogenetic photostimulation (onset: red bar) on the 400 μm spacing 32-channel SiMNA on at 8 DIV ($N = 20$). Blue circle indicates the approximate area of focus for the photostimulation beam; g,h), LFP; and i,j) MUA.

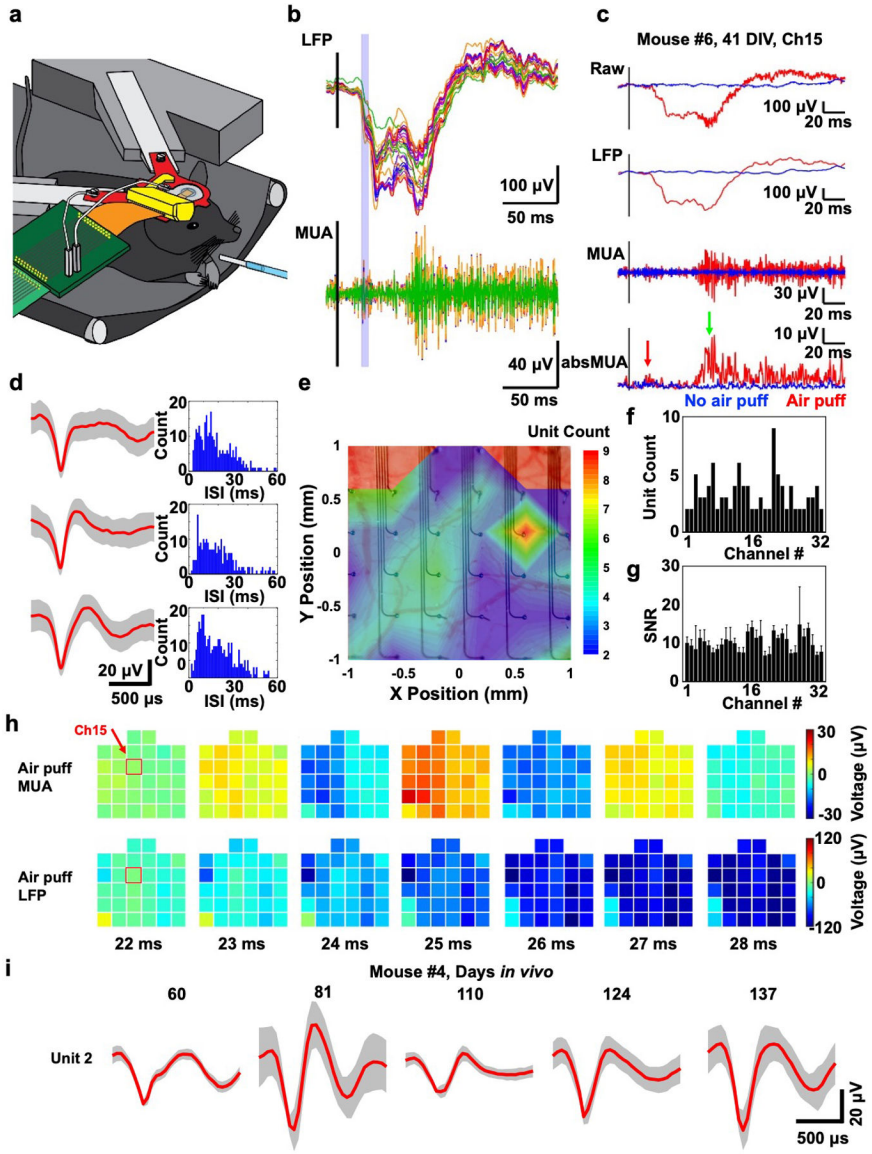

Figure 3.

In vivo whisker air puff stimulation-evoked responses at 41 DIV (mouse #6). a) Schematic illustration of the chronic in vivo recording setup showing on the right a glass tube for whisker air puff stimulation (blue). b) Average (N = 20) filtered whisker air puff stimulation-evoked responses from all channels of the 400 μm spacing 32-channel SiMNA on flex implanted on mouse somatosensory cortex. c) Average filtered whisker air puff stimulation-evoked responses from a single channel (Ch15). d) Three single units and corresponding interspike interval histograms detected from Ch15 of the same mouse. e) Colormap of number of detected single units per channel overlayed on the image of the implanted device. f) Histogram of number of detected single units per channel. g) Histogram of average SNR and standard deviation of air puff stimulation-evoked responses (unfiltered) for 32 channels (up to 54 DIV). h) Colormaps of the amplitude of filtered whisker air puff stimulation-evoked MUA and LFP responses at 22–28 ms poststimulus, corresponding to

blue highlighted region in b). Ch15 from c is highlighted (red box) at 22 ms poststimulus. b–h), LFP: 1–250 Hz, MUA: 250–3000 Hz, absMUA: rectified MUA, i) Single unit waveforms (type 2) detected from Ch32 of SiMNA implanted on mouse #4 from various measurement days.

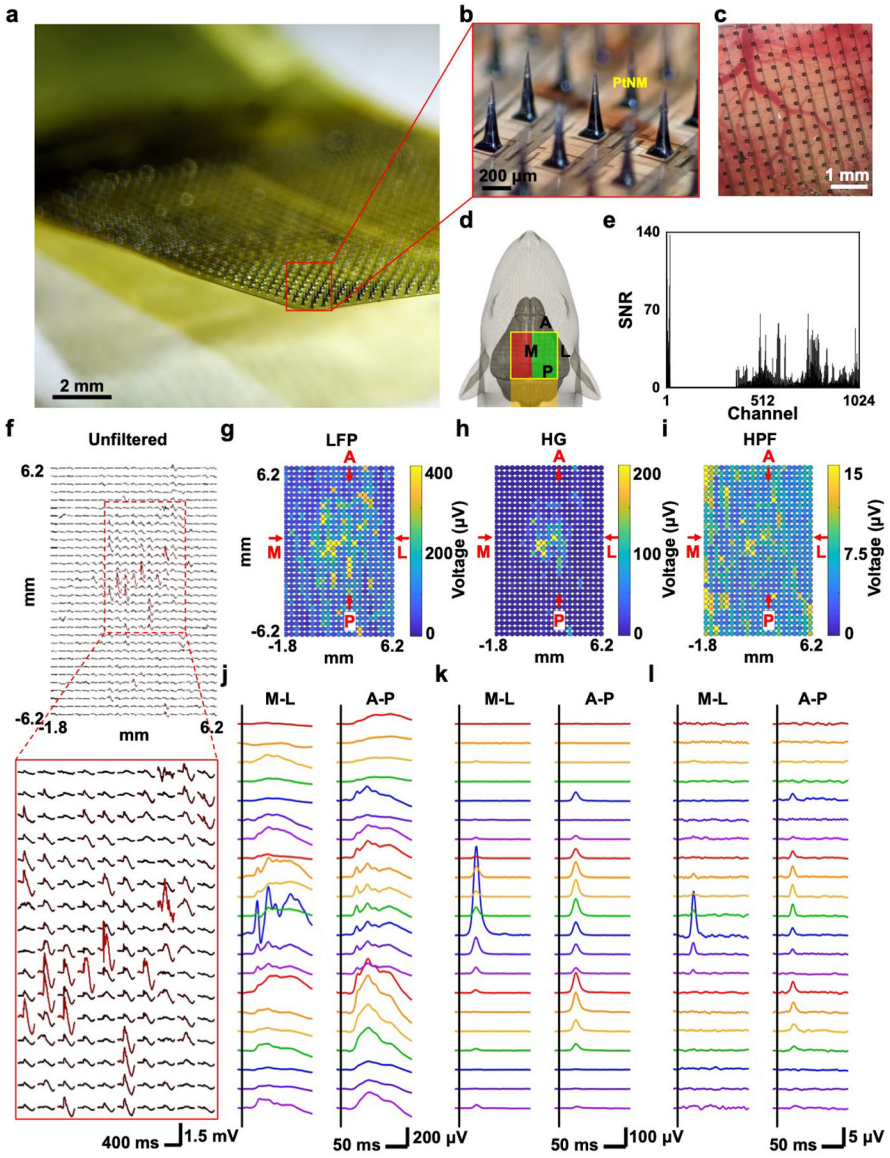

Figure 4.

1024-channel silicon microneedle array on flexible substrate (SiMNA on flex) for the detection of in vivo whisker air puff stimulation-evoked responses. a) A photograph of 1024-channel SiMNA on flex rested in mid-air. b) Magnified view of the array with SiMNs with tapered shape with height of about 300 μm and sharp tips coated with PtNM. c) Magnified view of the 1024-channel SiMNA implanted on the right hemisphere of rat brain. d) Schematic of implantation setup. Electrical connection is directed toward the posterior direction of the rat and the SiMNA is implanted in on the right hemisphere. The air puff is aimed on the contralateral whiskers. Green highlight region indicates the successfully implanted SiMN into the cortex, whereas the SiMNs in the red highlighted region are resting atop the rat skull. e) Histogram of SNR of whisker air puff stimulation-evoked LFP responses for 1024 channels (showing 672 channels from the green highlighted region from d) but excluding 352 channels from the red region from d). f) Mapping of unfiltered,

trial averaged, stimulation evoked waveforms. g–i) Colormaps of filtered whisker air puff stimulation-evoked LFP, HG, and HPF responses (average of 60 trials, LFP: 1–250 Hz, HG: 70–190 Hz, HPF: 250–3000 Hz). j–l) Filtered waveforms from medial (M)-lateral (L), and anterior (A)-posterior (P) cross-sections from corresponding colormaps in g–i) (average of 60 trials, LFP: 1–250 Hz, HG: 70–190 Hz, HPF: 250–3000 Hz).